

Positron emission tomography and single photon emission computed tomography imaging of tertiary lymphoid structures during the development of lupus nephritis

International Journal of
Immunopathology and Pharmacology
Volume 35: 1–13
© The Author(s) 2021
Article reuse guidelines:
sagepub.com/journals-permissions
DOI: 10.1177/20587384211033683
journals.sagepub.com/home/iji
SAGE

Esmail S Dorraji¹, Ana Oteiza², Samuel Kuttner² , Montserrat Martin-Armas², Premasany Kanapathippillai¹, Sara Garbarino³, Gustav Kalda², Mara Scussolini⁴, Michele Piana^{4,5} and Kristin A Fenton¹ 

Abstract

Lymphoid neogenesis occurs in tissues targeted by chronic inflammatory processes, such as infection and autoimmunity. In systemic lupus erythematosus (SLE), such structures develop within the kidneys of lupus-prone mice ((NZBXNZW)F1) and are observed in kidney biopsies taken from SLE patients with lupus nephritis (LN). The purpose of this prospective longitudinal animal study was to detect early kidney changes and tertiary lymphoid structures (TLS) using *in vivo* imaging. Positron emission tomography (PET) by tail vein injection of 18-F-fluoro-2-deoxy-D-glucose (¹⁸F-FDG)(PET/FDG) combined with computed tomography (CT) for anatomical localization and single photon emission computed tomography (SPECT) by intraperitoneal injection of ^{99m}Tc labeled Albumin Nanocoll (^{99m}Tc-Nanocoll) were performed on different disease stages of NZB/W mice (*n* = 40) and on aged matched control mice (BALB/c) (*n* = 20). By using one-way ANOVA analyses, we compared two different compartmental models for the quantitative measure of ¹⁸F-FDG uptake within the kidneys. Using a new five-compartment model, we observed that glomerular filtration of ¹⁸F-FDG in lupus-prone mice decreased significantly by disease progression measured by anti-dsDNA Ab production and before onset of proteinuria. We could not visualize TLS within the kidneys, but we were able to visualize pancreatic TLS using ^{99m}Tc Nanocoll SPECT. Based on our findings, we conclude that the five-compartment model can be used to measure changes of FDG uptake within the kidney. However, new optimal PET/SPECT tracer administration sites together with more specific tracers in combination with magnetic resonance imaging (MRI) may make it possible to detect formation of TLS and LN before clinical manifestations.

Keywords

systemic lupus erythematosus, lupus nephritis, tertiary lymphoid structures, positron emission tomography, single photon emission computed tomography, 18-F-fluoro-2-deoxy-D-glucose, ^{99m}Tc-Nanocoll

Date received: 17 December 2020; accepted: 21 June 2021

Introduction

Systemic lupus erythematosus is a systemic autoimmune disease characterized by the production of autoantibodies to nuclear self-antigens.^{1,2} In Lupus nephritis (LN) the formation of immune complexes and their consequent deposition within the kidney causes enhanced inflammation,

which leads to disruption of kidney integrity, and development of significant clinical proteinuria.^{3–7} The resulting proteinuria is often discovered too late to treat and save the kidneys. This can cause acute inflammatory lesions and chronic damage to the kidney and can cause the patient to require lifetime treatment, dialysis, or transplantation.^{4,5,8,9} To evaluate the progression of LN, a



Creative Commons CC BY: This article is distributed under the terms of the Creative Commons Attribution 4.0 License (<https://creativecommons.org/licenses/by/4.0/>) which permits any use, reproduction and distribution of the work without further permission provided the original work is attributed as specified on the SAGE and Open Access pages (<https://us.sagepub.com/en-us/nam/open-access-at-sage>).

renal biopsy is the gold standard, where a repeated biopsy often is required.^{10,11} Methods that can detect the early clinically silent events of LN are therefore highly needed.

Positron emission tomography is an *in vivo* imaging method commonly used in oncological applications, CNS, and cardiovascular imaging. One of the common tracers used in PET is the 18-F-fluoro-2-deoxy-D-glucose (¹⁸F-FDG). This tracer is taken up by cells that are highly glycolytic metabolically active. In addition to the neoplastic cells, immune cells, like macrophages and granulocytes, increase their expression of glucose transporters and glycolytic enzymes during phagocytosis.^{12,13} This makes the use of metabolic PET an interesting method in detecting activated immune cells *in vivo*. *Single photon emission computed tomography* (SPECT) is another *in vivo* imaging method with which ^{99m}Tc Albumin Nanocolloid has been used widely for the detection of the first drainage sentinel lymph nodes in cancer patients.^{14,15} The uptake is facilitated through phagocytosis by macrophages and granulocytes through phagocytosis specific receptors like the mannose receptor.^{16,17}

Lack of a non-invasive diagnostic test, which can diagnose LN at an early stage, is quite evident. *In vivo* molecular imagings such as PET and SPECT have been used widely to investigate normal and abnormal biological processes in different organs, but little work has been done for the kidney.^{18–20} The most used PET tracer is ¹⁸F-FDG, and different mathematical models of ¹⁸F-FDG have been developed to investigate the uptake in different organs.^{21–23} However, it has been difficult to design a model to evaluate renal FDG-PET data with regards to the complex structure of the kidney and the high excretion of FDG through the kidney.^{18,24,25}

The inflammatory aggregates observed during the progression of murine and human LN are organized into well-defined tertiary lymphoid structures (TLS).^{26–28} TLS form in tissues that are targeted by chronic inflammatory processes, such as infection and autoimmunity.^{29,30} We postulate that local events in the kidney, prior to

development of proteinuria, are the early but causal process in LN. We hypothesize that TLS formation can be used to detect a silent mesangial nephritis without renal clinical symptoms. Since TLS share similarities with lymph nodes regarding function and structure,³¹ the aim of this study was to use the of ¹⁸F-FDG in PET and ^{99m}Tc Albumin Nanocolloid in SPECT to investigate kidney functionality during SLE disease progression and facilitate the detection of the formation of TLS within the kidney of lupus-prone NZB/W mice, a model of SLE in humans.

Materials and methods

Calculation of sample size

This is a prospective longitudinal animal study. The amount of the animals was calculated based on the “resource equation” method using the equation: $E = \text{Total number of animals} - \text{Total number of groups}$. E is the degree of freedom of analysis of variance (ANOVA), and the value of E should lie between 10 and 20 (ref). The minimum number of animals in this study was calculated to be three in each group and maximum four when using six groups of animals.

Animals and grouping

20 BALB/c and 40 (NZBxNZW)F1(NZB/W) mice were purchased from Harlan (Harlan Sprague Dawley Inc, Indiana, USA). Forty-three of the mice were included for PET imaging, 19 mice for SPECT imaging and 16 mice for organ distribution. The Animal Welfare Board, at the UiT–The Arctic University of Norway and the regional ethical committee in Northern Norway approved all procedures (Reference number 6776).

The mice were divided into groups based on age, anti-dsDNA positivity and proteinuria. The groups consisted of 7 weeks old BALB/c (young BALB/c) ($n = 3$); 14–37 weeks old BALB/c (old BALB/c) ($n = 11$); 7 weeks old anti-dsDNA Ab negative NZBW (young Ab neg) ($n = 4$); 11–33 weeks old anti-dsDNA Ab negative NZBW (old Ab neg) ($n = 20$); anti-dsDNA Ab positive (being Ab positive for from 1 up to 6 weeks) (Ab+) ($n = 12$); and anti-dsDNA Ab positive (being Ab positive for from 7 up to 9 weeks) (Ab++) ($n = 11$). None of the mice included in PET or SPECT were proteinuric.

Anti-dsDNA Antibody enzyme-linked immunosorbent assay and measurement of proteinuria

The level of anti-dsDNA antibody in lupus-prone mice serum was measured as described previously.³² Blood samples were taken every week until positive ELISA test, and thereafter, every second week until proteinuria was

¹RNA and Molecular Pathology Research Group, Institute of Medical Biology, Faculty of Health Sciences, UiT The Arctic University of Norway, Tromsø, Norway

²Nuclear Medicine and Radiation Biology Research Group, Department of Clinical Medicine, Faculty of Health Science, UiT The Arctic University of Norway, Tromsø, Norway

³Centre for Medical Image Computing, Department of Computer Science, University College London, London, UK

⁴Dipartimento di Matematica, Università di Genova, Genova, Italy

⁵Dipartimento di Matematica, Università di Genova, and CNR-SPIN, Genova, Italy

Corresponding author:

Kristin A Fenton, RNA and Molecular Pathology Research Group, Institute of Medical Biology, Faculty of Health Sciences, UiT The Arctic University of Norway, MH Building, Tromsø 9037, Norway.
Email: kristin.fenton@uit.no

detected in urine. The protein in the urine was determined by urine dipstick (Bayer Diagnostics, Bridgend, United Kingdom): 0–1+ (<1 g/L) was regarded as physiological proteinuria; 2+ (≥ 1 –3 g/L) and 3+ (≥ 3 –20 g/L) and 4+ (≥ 20 g/L). Proteinuria was defined as 4+.

Animal preparation

Mice subjected to ^{18}F -FDG PET/CT imaging were fasted 3 h before acquisition, weighted, and anesthetized. Mice were anesthetized with isoflurane (induction 4% and maintenance 2% in oxygen). To prevent hypothermia, the temperature of the bed was set to 35°C during imaging procedure. For mice undergoing PET/CT imaging, a catheter with 30-gauge needle was placed into the mice lateral tail vein to allow tracer injection.

Imaging

PET, SPECT, and CT imaging were performed by using the Triumph™ LabPET-8™, 4-detector configuration X-SPECT® small animal PET/SPECT/CT scanner (Trifoil Imaging, Northridge Tri-Modality Imaging, Inc., Chatsworth, CA).

^{18}F -FDG PET/CT imaging

10.57 ± 1.79 MBq ^{18}F -FDG was diluted in 100 μl in sterile saline ($n = 103$) and injected through the lateral vein catheter using an automated infusion pump (0.2 ml/min). A 60-minute list mode PET acquisition was started simultaneously with the start of the ^{18}F -FDG injection. After PET acquisition, two CT scans were acquired at 80 kVp, 2×2 binning, 512 projections, and $1.3 \times$ magnification. The first was performed without contrast agent, and the second with 125 μl Iomeron350 (Bracco Imaging Scandinavia AB, Sweden) injected through the lateral vein catheter using an automated infusion pump over a 60 s period. The second CT scan started 2 min post-contrast agent injection.

The acquired list mode PET data were histogrammed into 24×5 s, 9×20 s, and 11×5 min, in total 44 time frames, and reconstructed using 3-dimensional maximum likelihood expectation maximization (MLEM) algorithm with 50 iterations. PET images were corrected for varying detector element efficiency, radioactive decay, random coincidences, dead time losses, attenuation, and scatter, before a dose calibration factor was applied, to convert the output images into the unit of MBq/cm³. CT raw data were reconstructed using filtered back projection algorithm.

$^{99\text{m}}\text{TC}$ -Nanocoll SPECT/CT imaging

Mice were anesthetized as described above and injected intraperitoneally (i.p.) with $^{99\text{m}}\text{TC}$ -Nanocoll (mean dose

activity 56.37 MBq \pm 9.1 MBq) diluted in sterile saline (100 μl maximum injection volume). Dynamic SPECT scans (60 min, 4×15 min time frames) started 12 ± 9 min post tracer injection. Acquisition was performed with 90° rotation, to cover one revolution with the four SPECT detectors, 16×4 projections, five multipinhole collimator (N5F75A10), and 45 mm radius of rotation. The images were reconstructed using ordered subset expectation maximization algorithm (eight subsets and five iterations). A CT scan was performed after SPECT acquisition, with identical acquisition parameters as for PET imaging, described above.

Data analysis of in vivo imaging

Kinetic analysis of PET data. Images were analyzed using PMOD (PMOD Technologies Ltd., Zürich). Volumes of interests representing whole kidney, cortex, and renal hilum were delineated in the CT images, and VOIs representing bladder were drawn in the PET images. These VOIs were outlined semi-automatically (60% isocontour of the maximal voxel value). ^{18}F -FDG blood concentrations were obtained from the vena cava VOI (1 mm³). This VOI was selected by finding the voxel with highest activity in the first 5–10 s of the PET scan (first or second time frame). Volumes of interest data were converted to standardized uptake value (SUV) g*min/ml) by normalizing to injection dose per animal weight. The area-under-curve (AUC) was calculated for renal hilum, cortex, and kidney tissue regions based on the measured time activity curves from each segmented region in the dynamic PET data.

Three-compartment model. A three-compartment model, based on work done by Qiao et al.,¹⁸ was implemented in an in-house developed MATLAB script (Mathworks, USA) (Figure 1a). The model equation is given by $C_T(t) = K_1 e^{-k_2 t} \otimes C_B(t) + f_1 C_B(t) + f_2 C_{\text{renal hilum}}$, where C_B is the input function, approximated by the image derived time activity curve (TAC) from the vena cava region. C_1 and C_2 , corresponding to the activity concentration in parenchyma and urine, respectively, were estimated from kidney cortex and urine in renal hilum and bladder TACs, respectively. C_T is the concentration of FDG measured in the kidneys from PET. The model was fitted to the data using a nonlinear least-squares solver (lsqcurvefit). The resulting model parameters K_1 and k_2 , the fractional calibration factors f_1 and f_2 , and the coefficient of determination, r^2 , were extracted and compared between different age and disease stage groups of animals.

Five-compartment model. The five-compartment model (Figure 2a), described by Garbarino et al.,³³ consists of C_m : a compartment involving the ^{18}F -FDG-6-phosphate, the FDG in cells, and the pre-urine pool accounting for tracer

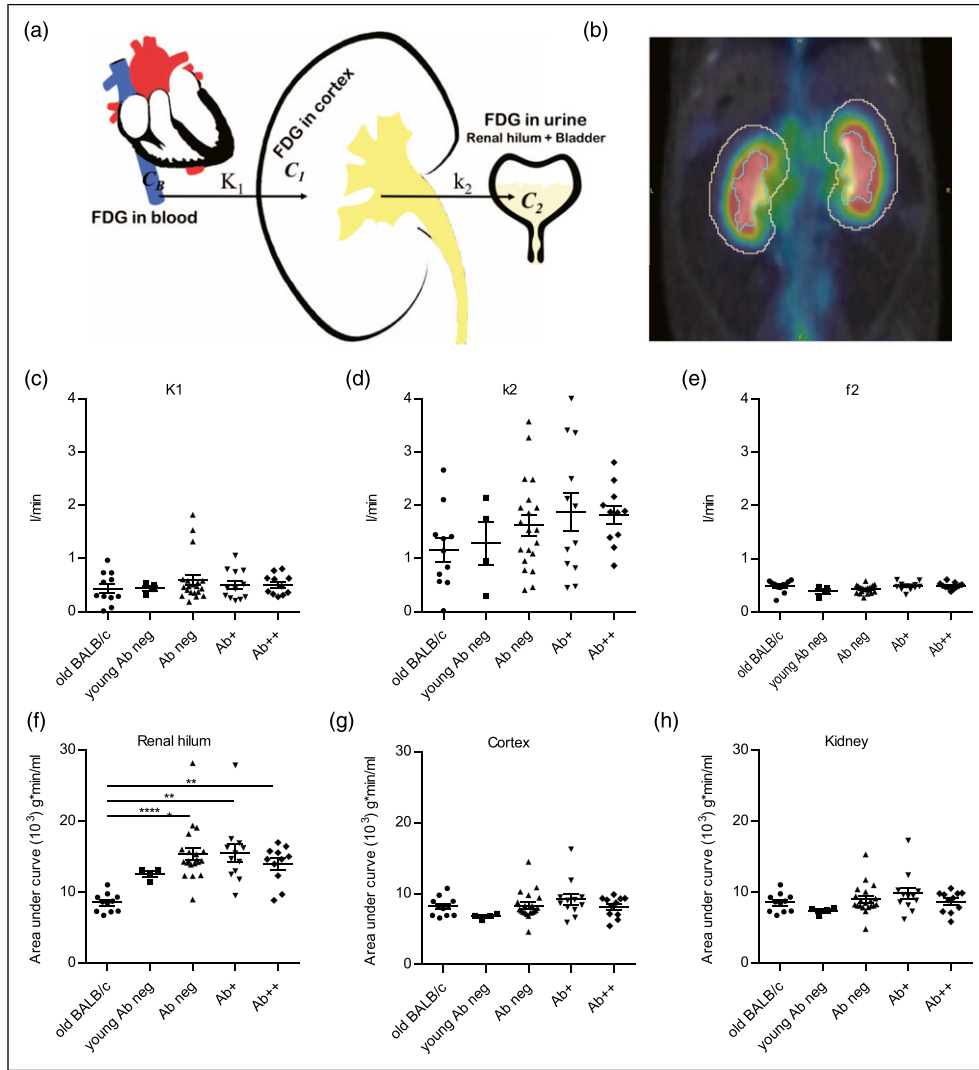


Figure 1. Renal hilum SUV increased in anti-dsDNA Ab+ mice. (a) Illustrates the three-compartment model. C_B , C_1 , and C_2 represent tracer in the blood (input function), activity concentration in the parenchyma, and urine, respectively. (b) Cortex and renal hilum were delineated based on CT. There was no difference in K_1 (c) and f_2 (e) between the groups, but k_2 (d) increased during SLE progression. Area-under-curve of renal hilum (f) increased during SLE progression, while AUCs of cortex (g) and whole kidney (h) were steady. (c)–(h) One-way ANOVA with post-hoc analysis (Dunn's multiple comparisons test). * $p < 0.05$, ** $p < 0.01$, *** $p < 0.001$, **** $p < 0.0001$.

filtered in the pre-urine and entering the proximal tubule. This compartment contains the majority of tracer in the kidneys, which is defined as a metabolized compartment to indicate the fact that the FDG can also be in the ^{18}F -FDG-6-phosphate form in this state. C_a : vena cava compartment, which includes tracer in blood flow that later enters to the kidney. C_f : an extravascular compartment in the kidney representing the free tracer outside cells, where they exchange with vena cava and metabolized compartments. C_i : the tubular compartment, in which tracer concentration can vary because of water reabsorption. C_u : accounting for the ultimate tracer excretion, which has been measured in urine in the bladder.

The exchange rates are denoted as k_{XY} , where X indicates the compartment of destination and Y the compartment of origin. Simple balance of tracer leads to the following set of equations

$$C_f = -(k_{af} + k_{mf})C_f + k_{fm}C_m + k_{fa}C_a$$

$$C_m = k_{mf}C_f - (k_{fm} + k_{tm})C_m + k_{ma}C_a$$

$$C_t = -k_{ut}C_t + k_{tm}C_m$$

The total concentration of tracer in the kidneys, C_K , can be written as (Kimura et al. ³⁴)

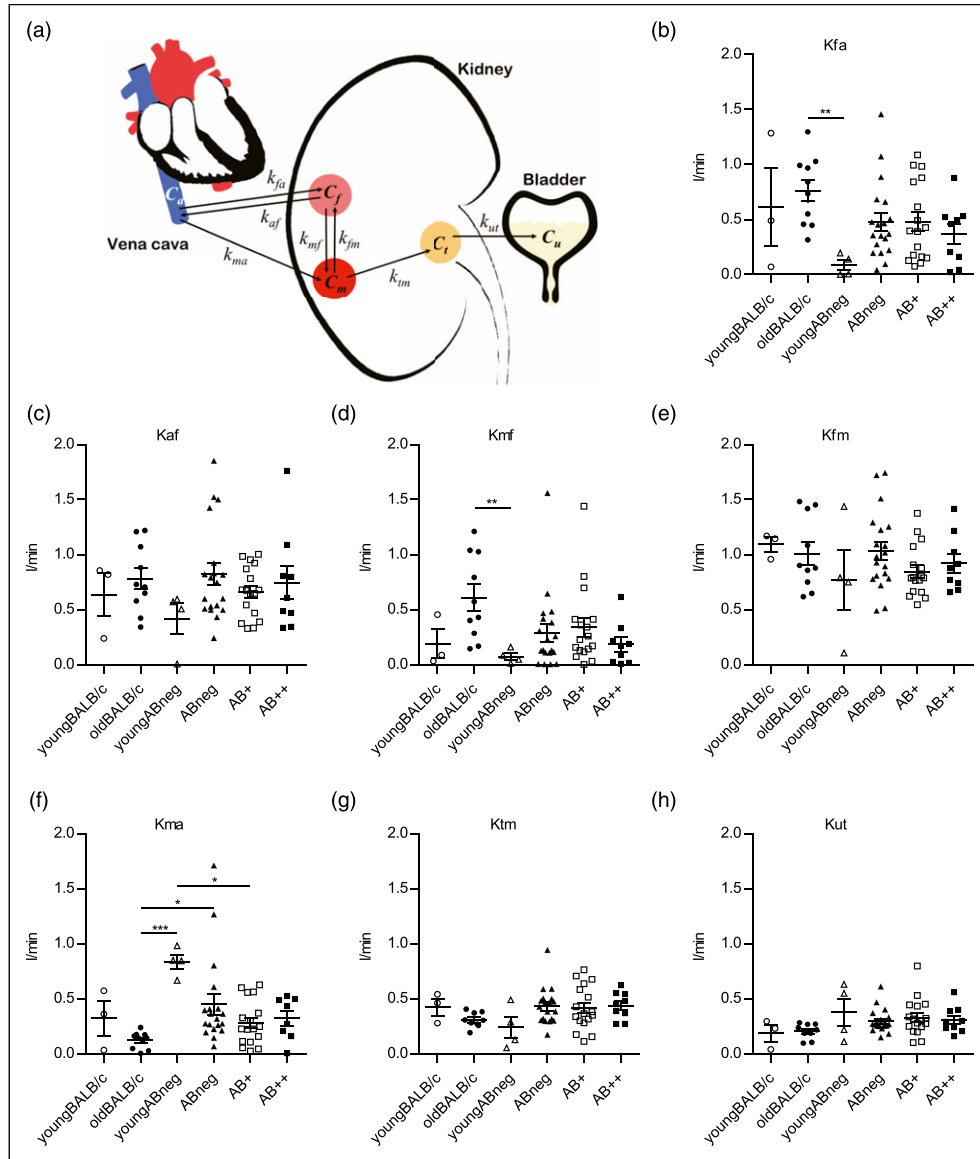


Figure 2. Filtration of ^{18}F -FDG by glomeruli was lower in lupus-prone mice producing anti-dsDNA Ab. (a) Illustrates the five-compartment model, where C_a , C_f , C_t , C_u , and C_m represent tracer in blood, extravascular, tubule, urine, and metabolized ^{18}F -FDG, respectively. The k_{fa} (b), k_{af} (c), and k_{mf} (d) were increased in mice with anti-dsDNA Ab production, but k_{ma} (f) decreased. k_{fm} (e), k_{im} (g), and k_{ut} (h) were steady during SLE progression. (b)–(h) One-way ANOVA with post-hoc analysis (Dunn's multiple comparisons test). * $p < 0.05$, ** $p < 0.01$, *** $p < 0.001$.

$$C_K = \eta_a C_a + (1 - \eta_a - \eta_t)(C_f + C_m) + C_t \eta_t$$

where η_t and η_a are the fractions of kidney volumes V_K occupied, respectively, by the tubular compartment and the blood. The model was implemented in an in-house developed MATLAB script. Groups of mice consisted of youngBALB/c ($n = 3$), oldBALB/c ($n = 10$), young Ab neg ($n = 4$), Ab neg ($n = 19$), AB+ ($n = 17$), and AB++ ($n = 9$).

SPECT/CT data analysis. The images obtained from $^{99\text{m}}\text{Tc}$ -Nanocoll dynamic SPECT were visually evaluated by three

nuclear medicine *specialists* to identify the accumulation of the colloid in the different organs in different groups: BALB/c ($n = 3$), anti-dsDNA Ab- ($n = 8$), and anti-dsDNA Ab++ ($n = 10$). Volumes of interests were drawn automatically in the entire mouse in the 4th SPECT time frame. This was achieved by using 3D automatic segmentation at 25% threshold of the maximum signal inside the mouse body. All VOIs were quantified by mean pixel intensity, and those with accumulation of $^{99\text{m}}\text{Tc}$ -Nanocoll over time were selected for further analysis (Supplementary Figure S1).

Ex vivo organ biodistribution

The anesthetized animals were euthanized by cervical dislocation 1 h after ^{18}F -FDG injection. Internal organs were collected, rinsed ($2\times$ deionized water), weighted, and measured for radioactivity in an automatic gamma counter (2480 Wizard, PerkinElmer, MA, USA). Organ SUVs were calculated as described above.

Immunohistochemistry

Hematoxylin and eosin (H&E) staining, Alcian blue/periodic acid-Schiff (AB/PAS) staining, and detection of CD3 positive T cells (Dako, 3 $\mu\text{g}/\text{ml}$), B220 positive B cells (R&D systems, 0.83 $\mu\text{g}/\text{ml}$), and F4/80 positive macrophages (Biolegend, 1 $\mu\text{g}/\text{ml}$) in 4 μm paraffin embedded kidney sections were performed as described previously.^{28,35} Envision+ system-HRP/DAB anti-rabbit detection kit (K4011, Dako) was used to detect CD3, and Polink-2 Plus HRP anti-rat DAB detection kit (D46-15, Golden Bridge International) was used to detect B220 and F4/80.

Autoradiography

Mice were anesthetized with isoflurane and buprenorphine injected subcutaneously (Temgesic, 0.1 mg/kg body weight). Following $^{99\text{m}}\text{Tc}$ -Nanocoll SPECT/CT imaging, *ex vivo* autoradiography of pancreas was performed. A blood sample was collected by cardiac puncture, and mice were euthanized by blood loss under anesthesia. Subsequently, pancreas was removed, embedded in Tissue-Tek[®] O.C.T. (Sakura-Finetek, USA), and frozen on dry ice. Sections (-20°C , 20 μm thick) were prepared by a cryostat and thaw-mounted on Superfrost[®] Plus glass slides (Carl Roth GmbH & Co. KG, Karlsruhe, Germany). Sections were thawed and dried for 30 minutes at 22°C . Slides were exposed to a phosphor storage screen inside a cassette overnight at 21°C . Images were developed using a Cyclone Plus storage phosphor system (Perkin Elmer, MA, USA), and the results were evaluated using Image J software (National Institutes of Health, MD, USA). A calibration factor was calculated after counting the radioactivity in the blood samples and normalizing to injection dose per animal weight. Image pixel values were converted to SUV.

Reagents and antibodies

^{18}F -FDG was provided by the University hospital of Northern Norway (UNN)(MAP Medical Technologies, Finland). $^{99\text{m}}\text{Tc}$ and Nanocoll were purchased from GE Healthcare (USA). CD3 rabbit-anti-mouse (AD452) was purchased from Dako (Denmark), B220 rat-anti-mouse (MAB1217) from R&D Systems (USA), and F4/80 rat-anti-mouse (122603) was obtained from Biolegend (USA).

Statistical analysis

One-way ANOVA with post-hoc analysis (Dunn's multiple comparisons test) was performed for PET and SPECT, and unpaired t test was performed on *ex vivo* organ biodistribution data. A p -value of ≤ 0.05 was considered statistically significant, and data are presented as mean \pm SEM. Statistical analysis was performed with GraphPad Prism (GraphPad Software, CA, USA).

Results

Decreased glomerular filtration was detected by ^{18}F -FDG PET during early SLE progression

To investigate kidney functionality during SLE disease progression, dynamic PET/CT was performed on different groups of lupus-prone mice (NZBW F1) and control BALB/c mice. The 3CM, using vena cava, kidney, and urine, was used to analyze the data (Figure 1a). Two VOIs, cortex and renal hilum, were defined in kidneys based on the CT (Figure 1b). The K_1 and f_2 generated with MATLAB 3CM were the same in BALB/c and NZBW at the different stages of disease (Figure 1c and e). The k_2 increased synchronously with disease progression in NZBW mice, and the highest levels were observed in the Ab+ and Ab++ groups. The AUC of the renal hilum was higher in Ab neg, Ab+, and Ab++ compared to young Ab neg and significantly higher compared to old BALB/c (Figure 1f). There were no significant differences of AUC for the cortex and the whole kidney (Figure 1g and h, respectively).

To determine the best possible compartment model to evaluate the kidney functionality during SLE disease progression, data generated through dynamic PET were analyzed by the 5CM (Figure 2a). The k_{fa} , k_{af} , and k_{fm} were higher in Ab neg, Ab+, and Ab++ groups compared to young Ab neg group (Figure 2b–d). A significantly lower level of k_{ma} was observed in Ab+ compared to young Ab neg, and it was notably lower in Ab neg compared to young Ab neg (Figure 2f). The k_{mf} , k_{m} , and k_{ut} were relatively the same in Ab neg, Ab+, Ab++, and young Ab neg groups (Figure 2g and h). The mean k values with SEM for 1 BALB/c and 3 different NZB/W mice are shown in Supplementary Figure S2.

^{18}F -FDG accumulate highly in lymph nodes of anti-dsDNA Ab+ Mice

Ex vivo organ biodistribution studies after dynamic PET were performed on BALB/c ($n = 6$), Ab neg ($n = 2$), and Ab+ ($n = 3$) mice to examine ^{18}F -FDG accumulation in different organs of different groups of mice (Figure 3a). We observed a notable higher ^{18}F -FDG accumulation in the heart (Figure 3b) renal lymph nodes (Figure 3c), axillary/brachial lymph nodes, right and left kidneys (Figure 3d and e,

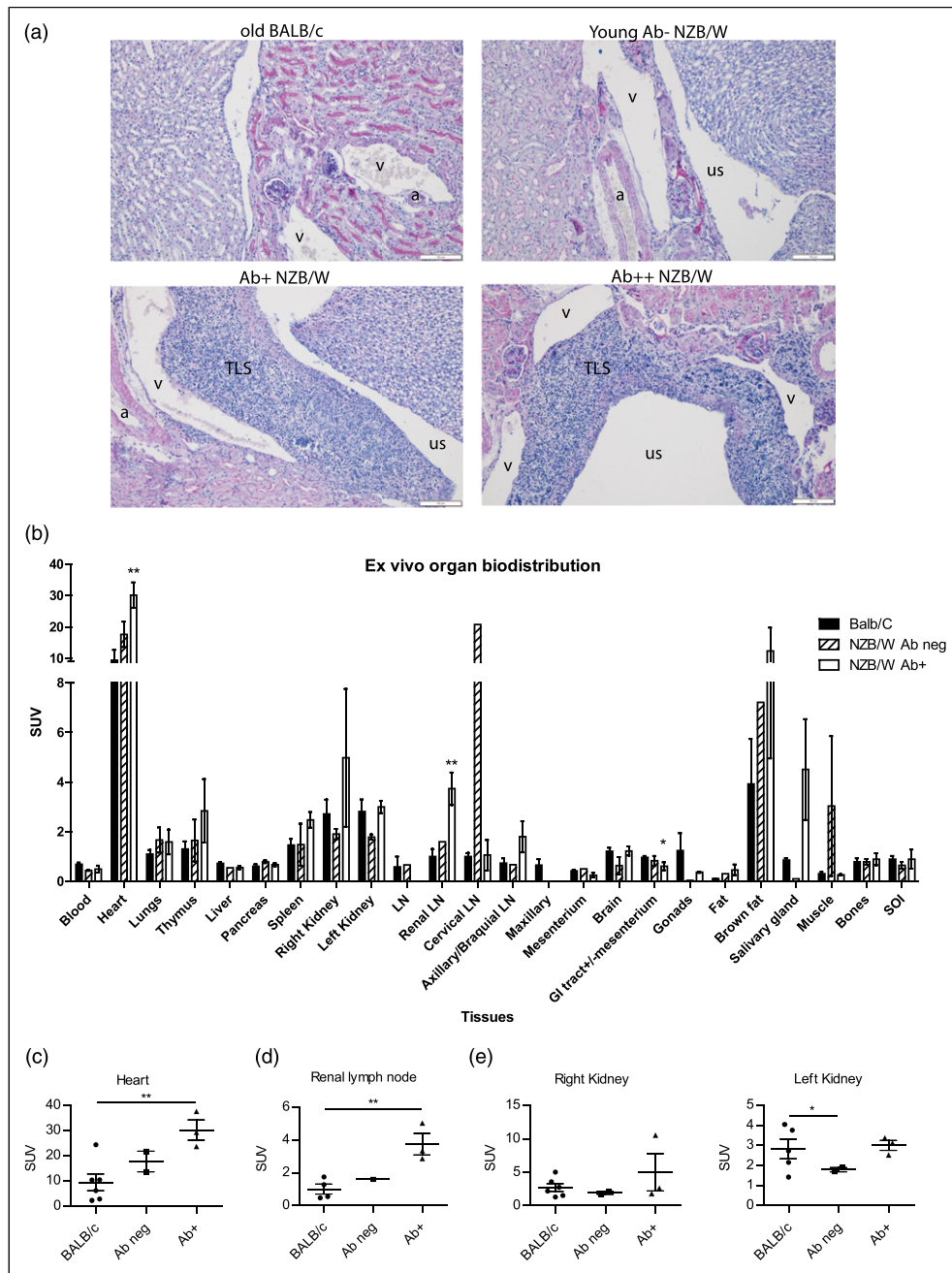


Figure 3. Histological pictures and ex vivo organ biodistribution. (a) Representative Alcian blue/periodic acid-Schiff (AB/PAS) stained kidney sections from old BALB/c, Ab- NZB/W, Ab+ NZB/W, and Ab++ NZB/W mice. (b) ^{18}F -FDG accumulation measured by SUV (g/ml) in tissue after 24 h. ^{18}F -FDG accumulated higher in heart (c) and renal lymph node (d). ^{18}F -FDG was higher in right (e) and left (f) kidneys, axillary/brachial lymph node, spleen, thymus, and salivary gland (b) of anti-dsDNA Ab+ mice compared to Ab neg mice and was lower for GI track (b). Unpaired *t* test. * <0.05 , ** <0.01 . a, artery; us, urinary space; v, vein. Scale bar = 100 μm .

respectively), spleen, thymus, and salivary gland in Ab+ compared to Ab neg mice (Figure 3a). The SUV value for gastrointestinal tract was significantly lower in Ab+ NZB/W compared to BALB/c and moderately lower compared

to Ab neg mice (Figure 3a). Standardized uptake value measured in gonad, brown fat, fat, liver, lung, muscle, bone, pancreas, and SOI was relatively the same between the groups (Figure 3a).

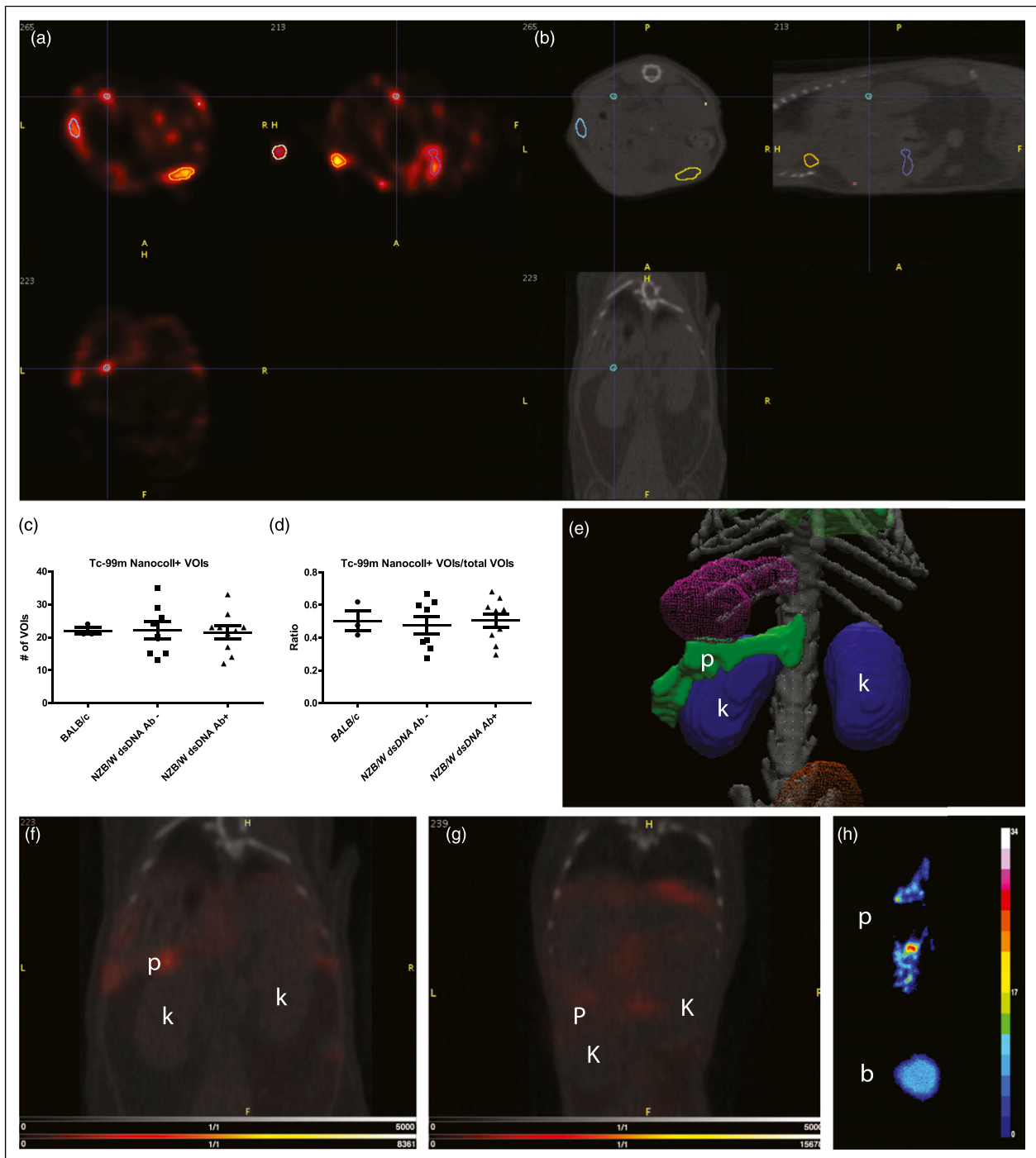


Figure 4. SPECT imaging of pancreatic TLS. (a) SPECT and (b) CT transversal, coronal, and sagittal frames of an example (dsDNA Ab+) showing multiple ROIs generated in Pmod 3.7. A threshold of 75% of the maximum activity was defined for the delineation in all mice. (c) Total number of VOIs accumulating ^{99m}Tc -Nanocol over time in BALB/c, dsDNA Ab- NZB/W, and dsDNA Ab+ NZB/W groups. (d) Relation between total number of VOIs drawn and the number of VOIs that accumulated ^{99m}Tc -Nanocol with time. No differences among the groups could be observed. (e) Atlas representation of kidneys and pancreas in the mouse. (f) Representing a fusion SPECT/CT image of the NZB/W dsDNA Ab+ mouse with a hot spot in the pancreatic area, which could only be observed in NZB/W dsDNA Ab+ mice ($n = 6$) not in the (g) BALB/c or NZB/W dsDNA Ab neg mice (data not shown). (h) Autoradiography of the ^{99m}Tc Nanocol in dsDNA Ab+ mice, which shows a clear tracer accumulation in the pancreas in comparison to blood. (c)–(d) One-way ANOVA with post-hoc analysis (Dunn's multiple comparisons test). p, pancreas; k, kidney; b, blood.

^{99m}Tc-Nanocoll SPECT can visualize organ-specific TLS

The ^{99m}Tc-Nanocoll was used to investigate the presence of TLS in organs of lupus-prone mice at different stages of disease progression. We observed no differences among the total number of VOIs automatically drawn by the software in the different groups, and no differences in the number of VOIs positively accumulating Nanocoll with time among the groups (Figure 4a–d). Through all the positive VOIs within the different groups, only the VOI which was drawn in the pancreatic area varied between groups. The pancreatic VOI was only observed in the dsDNA Ab+ group (6 out of 11 mice), which was selected due to its notable high signal intensity (Figure 4f). We did not observe the same observation in the anti-dsDNA Ab neg and BALB/c groups (Figure 4g).

The ex vivo autoradiography following dynamic SPECT was performed to confirm the accumulation of ^{99m}Tc-Nanocoll in pancreas of anti-dsDNA Ab+ ($n = 4$) and BALB/c ($n = 2$) groups. We detected the accumulation of colloid in pancreas of dsDNA Ab+, but not in BALB/c (Figure 4h). We performed HE staining and IHC detecting T cells, B cells, and macrophages on pancreatic sections from NZB/W and BALB/c mice (Figure 5). In the mice with positive SPECT signals, we found TLS within the

pancreas (Figure 5a–c). The TLS were detected within stromal areas (Figure 5a and b), but also within the pancreatic tissue close to the larger arteries and veins (Figure 5c). The BALB/c mice did not show any infiltration of aggregated immune cells (Figure 5d).

Discussion

In this study, we have performed dynamic PET-CT, SPECT-CT, ex vivo organ biodistribution, and autoradiography on lupus-prone mice at different stages of the disease to develop non-invasive molecular imaging techniques to visualize TLS, measure changes in FDG uptake, and diagnose LN at an early stage. The AUC-SUV for renal hilum and SUV value for k2 (urinary clearance of FDG) increased during LN progression. Hao et al.¹⁸ have reported a decline in the time of FDG clearance in anti-GBM nephritic mice by disease progression, but they did not evaluate the level of FDG clearance regardless of the time. In the 3CM model, the metabolized FDG was neglected based on the small amount compared to FDG in urine or free FDG.¹⁸ In a healthy kidney, it might be correct, but in autoimmune patients with progressive nephritis owing to a large population of cells with high metabolic needs such as activated macrophage, B cell and T cell in the kidney,^{36,37} the metabolized FDG cannot be ignored. The 3CM model

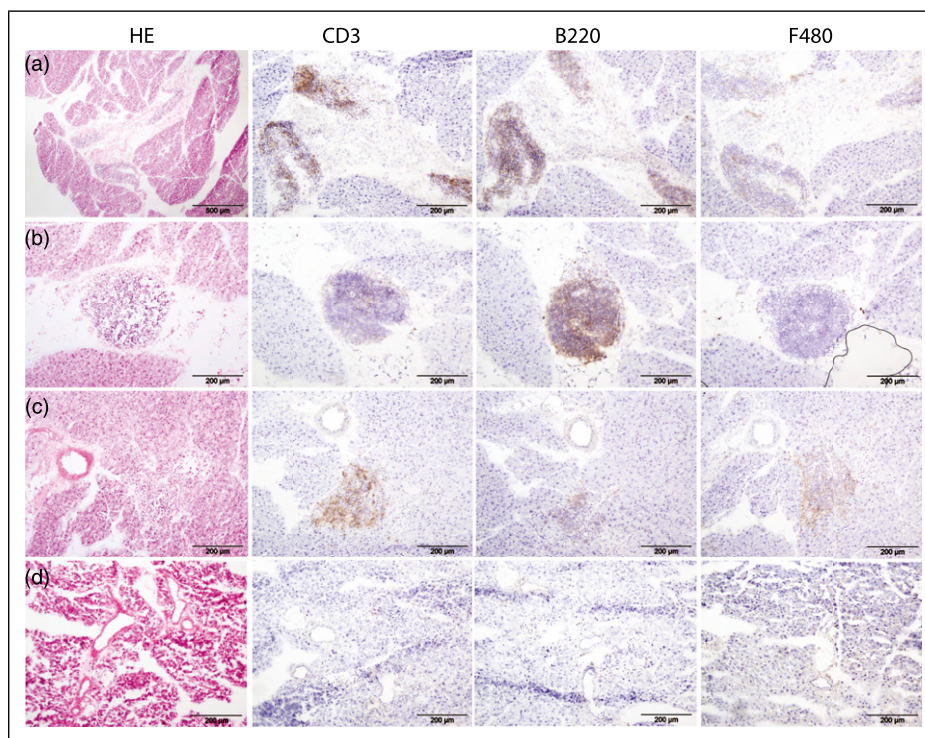


Figure 5. HE staining and immunostaining of TLS in pancreatic tissue in lupus-prone (a)–(c) and BALB/c mice (d). TLS was positively stained for T cells (CD3), B cells (B220), and macrophages (F480). Some TLS was detected near pancreatic islets (black arrows, c). (d) TLS was not detected in pancreatic sections from BALB/c mice. a, artery; d, ducts.

was developed based on human kidneys and regard to the fundamental differences between human and mouse kidney; this model might not be the best choice for evaluating preclinical FDG-PET data.

The majority of previous renal system compartment models have defined two functional compartments, which are anatomically embedded.³³ However, 5CM in this study introduces the tubular (functional and anatomical) and bladder (anatomical) compartments.³³ Garbarino et al.³³ designed the model based on an increase of k_{ut} compared to k_{tm} by the factor of 10 due to water reabsorption in the tubule. In the 5CM in this study, the volume of water and kidney is considered as a fixed value. Thus, k_{ut} will not increase compared to k_{tm} due to water reabsorption. Since the tracer will not be reabsorbed in the tubule and we have a fixed value for the volume of water and kidney, k_{tm} and k_{ut} should represent relatively the same level as we observed in our data. We consider it as a validation for the persistent accuracy of data generated by the 5CM model.

Through extensive glomerular damage in LN, the glomerular filtration is disturbed by disease progression.^{37,38} In the 5CM, the k_{ma} is described as glomerular filtration. The notable decline that we observed in glomerular filtration of FDG in older Ab neg mice compared to young Ab neg mice can be considered as an early diagnostic sign of nephritis, which decreased significantly by disease progression, without clinical symptoms. Metabolized ^{18}F -FDG (^{18}F -FDG-6-phosphate) can stay in cells (C_m) until the ^{18}F decays and converts to ^{18}O , and ^{18}O -glucose-6-phosphate can be metabolized as ordinary glucose or it can be transferred to the interstitial space (k_{fm}). We did not observe significant changes in k_{mf} and k_{fm} ($C_f \rightleftharpoons C_m$) during early LN progression. A weakness of this model is that it does not consider the lymphatic pharmacokinetics within the kidneys.

Systemic lupus erythematosus is an autoimmune disorder, which immune cells in secondary lymphoid organs (SLO), lymph nodes, and spleen are in an active stage. Ex vivo organ biodistribution showed higher FDG accumulation in organs with higher immune cell compositions such as lymph nodes, spleen, and thymus compared to other organs like brain, liver, and lungs. It has been reported that LN patients develop TLS in the kidney,^{39,40} and based on our finding, anti-dsDNA Ab positive lupus-prone mice develop TLS within the kidney, and when they become proteinuric, a large and organized TLS with germinal center-like structures develop within the kidney.^{26,28} In this study, we observed higher ex vivo FDG accumulation in the kidney of anti-dsDNA Ab positive groups compared to Ab neg mice, which are in accordance with the presence of large population of metabolic active or activated immune cells. However, the tracer was injected intravenously (i.v.), and it is unclear if this route of administration will reach the developing TLS within the kidney or other organs. Based on our previously published research, the TLS develop in

near proximity to the biggest veins and arteries and contain lymph vessels and micro capillaries.^{26,28} The larger renal drainage lymphatics in mice can be found in the same hilar area.^{28,41} However, it is still unknown if the blood flow in TLS is connected to the larger vessels. Very little is known about the lymphatic flow within TLS.⁴² Based on our results, it seems like the tracer did not reach the TLS. To detect formation of TLS within the kidney, more knowledge about the lymphatics within the kidney and possible injection sites to reach them are needed.

TLS resemble SLO regarding structure, cell composition, and function.³¹ Labeled radiotracers up to about 100 nm can enter the lymphatic capillaries and be transported to lymph nodes.⁴³ More than 95% of the nanocolloidal albumin particles are up to 80 nm, which make them an excellent candidate to study lymph nodes with high uptake rate.^{44,45} Our data showed accumulation of $^{99\text{m}}\text{Tc}$ Nanocoll in the lymph nodes and spleen after 1 h. Several studies have reported pancreatic TLS contains T and B cell zones, HEVs, plasma cells, DCs, and HEVs in different mice models.⁴⁶⁻⁴⁹ We demonstrated for the first time that $^{99\text{m}}\text{Tc}$ Nanocoll accumulated in the pancreas of anti-dsDNA Ab positive NZB/W mice. The TLS within the pancreas was positively immune stained for macrophages, T and B cells, especially those located in the edge of the pancreas. Immune aggregates within the pancreas have been reported in NZB and NZB/W mice.⁵⁰ Several studies have previously reported incidences of pancreatitis in SLE patients,⁵¹ and some SLE patients had initial pancreatitis as an early manifestation of the disease.⁵² As for the pathogenic role of TLS and pancreatitis in murine SLE, the immune infiltrates were found around the pancreatic ducts, arteries, and veins and not close to the islets.⁵⁰ This is not in accordance with our study where TLS was located close to islets. In the previous studies, most of animals and patients had normal glucose levels, and most of the patients responded well to anti-inflammatory treatments.⁵³ Hence, the development of TLS within the pancreas of lupus-prone mice and SLE patients may reflect the systemic inflammatory disease caused by autoantibody binding in arteries and veins. We could not detect increased uptake of $^{99\text{m}}\text{Tc}$ Nanocoll in TLS within the kidneys. This could be due to the i.p. injection of the tracer or more likely due to the location of the TLS within the kidneys. Since the mice investigated had large TLS within the kidney, the i.p. injected tracer most likely did not reach the structure. This could be because of the direction of the blood and lymphatic flow within the kidney as discussed for the PET data. However, more studies on TLS formation in SLE are needed.

There are limitations in our study. The ^{18}F FDG tracer has a limitation of use because of the relatively short half-life. This, together with the clearance of tracer by the kidney, makes it difficult to measure and visualize uptake

of the tracer within structures of the kidney. In addition, the selected site of injection for both the PET and SPECT tracers may not be optimal for reaching the TLS within the kidney. In rodents, i.p. of macromolecules is typically taken up by the peritoneal lymphatics which directly drain into the thoracic duct and then empties into the venous blood supply.⁵⁴ The renal lymphatics are bypassed by this route of administration, and the spleen that filters the blood therefore picks up these nanocolloids and delivers them to the pancreaticosplenic lymphatics, which is where we visualized TLS. Given the organization of the lymphatics with respect to the hemovascular system, the bioavailability to the kidney lymphatics is quite low with i.p. or i.v. administration. TLS have HEVs that are specialized for naive T and B cell entrance,²⁸ and hence, the blood vasculature may not be an appropriate route for administration for evaluating TLS. Lymph always empties into the blood stream; it is not circulatory but rather unidirectional; and hence TLS identification in the kidney may require more careful consideration of route of administration. Our data indicate that there is a lack of lymphatic watersheds to the kidneys while the spleen lymphatics drain to the pancreatic lymphatics, explaining the tracer uptake within TLS in the pancreas. However, it is still unknown if the use of a long-lived tracer will omit the problem visualizing the uptake of tracer within TLS. The structure of the TLS developing within the kidney is relatively large compared to the whole kidney and is different in cellular density. This opens for the use of magnetic resonance imaging (MRI) in detecting TLS. Either alone or in combination with more specific tracers or appropriate injection sites.

We did not use power calculations to estimate the sample size. However, since it was not possible to assume the standard deviation and the effect size, we used the “resource equation” approach as an alternative approach to the power analysis.

Conclusion

The new 5CM demonstrated a significant change in the uptake of FDG in kidney of non-proteinuric anti-dsDNA Ab positive mice compared to healthy control mice. We were not able to in vivo visualize TLS within the kidney of lupus-prone NZB/W mice neither by PET nor SPECT using i.v. and i.p. injection of ¹⁸F FDG and ^{99m}Tc Nanocoll, respectively. However, we observed positive uptake of ^{99m}Tc Nanocoll by cells within pancreatic TLS. New long-lived specific tracers in combination with MRI, along with optimal injections sites, detecting the formation of TLS, may lead to early detection of LN prior to clinical manifestations.

Declaration of conflicting interests

The author(s) declared no potential conflicts of interest with respect to the research, authorship, and/or publication of this article.

Funding

The author(s) disclosed receipt of the following financial support for the research, authorship, and/or publication of this article: This project was funded by Northern Norway Regional Health Authority research grant SFP1263-15.

Ethics approval

Ethical approval for this study was obtained from The Animal Welfare Board, at the UiT–The Arctic University of Norway and the regional ethical committee in Northern Norway approved all procedures (Reference number 6776).

Animal welfare

The present study followed international, national, and/or institutional guidelines for humane animal treatment and complied with relevant legislation.

ORCID iDs

Samuel Kuttner  <https://orcid.org/0000-0001-7747-9003>
 Kristin A Fenton  <https://orcid.org/0000-0002-8356-2628>

Supplemental material

Supplemental material for this article is available online.

References

1. Lahita R (1999) The clinical presentation of systemic lupus erythematosus. In: Lahitha R (ed) *Systemic Lupus Erythematosus*. 3rd edition. San Diego, CA: Academic Press, 325–336.
2. Liu Z and Davidson A (2012) Taming lupus—a new understanding of pathogenesis is leading to clinical advances. *Nature Medicine* 18: 871–882.
3. Balow J, Boumpas D and Austin H III (2004) Systemic lupus erythematosus and the kidney. In: Lahita RG (ed) *Systemic Lupus Erythematosus*. 4th edition. New York, NY: Elsevier academic press, 877–912.
4. Chan TM (2015) Treatment of severe lupus nephritis: the new horizon. *Nature Reviews Nephrology* 11: 46–61. DOI: [10.1038/nrneph.2014.215](https://doi.org/10.1038/nrneph.2014.215).
5. Davidson A and Aranow C (2010) Lupus nephritis: lessons from murine models. *Nature Reviews Rheumatology* 6: 13–20. DOI: [10.1038/nrrheum.2009.240](https://doi.org/10.1038/nrrheum.2009.240).
6. Nangaku M and Couser WG (2005) Mechanisms of immune-deposit formation and the mediation of immune renal injury. *Clinical and Experimental Nephrology* 9: 183–191. DOI: [10.1007/s10157-005-0357-8](https://doi.org/10.1007/s10157-005-0357-8).

7. Anders H-J and Rovin B (2016) A pathophysiology-based approach to the diagnosis and treatment of lupus nephritis. *Kidney International* 90: 493–501. DOI: [10.1016/j.kint.2016.05.017](https://doi.org/10.1016/j.kint.2016.05.017).
8. Neild GH (2017) Life expectancy with chronic kidney disease: an educational review. *Pediatric Nephrology* 32: 243–248. DOI: [10.1007/s00467-016-3383-8](https://doi.org/10.1007/s00467-016-3383-8).
9. Mortensen ES, Fenton KA and Rekvig OP (2008) Lupus nephritis: the central role of nucleosomes revealed. *The American Journal of Pathology* 172: 275–283.
10. Hao G, Du Y, Zhou XJ, et al. (2013) Serial non-invasive assessment of antibody induced nephritis in mice using positron emission tomography. *PLoS One* 8: e57418. DOI: [10.1371/journal.pone.0057418](https://doi.org/10.1371/journal.pone.0057418).
11. Alsuwaida AO (2013) Interstitial inflammation and long-term renal outcomes in lupus nephritis. *Lupus* 22: 1446–1454. DOI: [10.1177/0961203313507986](https://doi.org/10.1177/0961203313507986).
12. Chan WK, Au WY, Wong CY, et al. (2010) Metabolic activity measured by F-18 FDG PET in natural killer-cell lymphoma compared to aggressive B- and T-cell lymphomas. *Clinical Nuclear Medicine* 35: 571–575. DOI: [10.1097/RLU.0b013e3181e4dcbf](https://doi.org/10.1097/RLU.0b013e3181e4dcbf).
13. Laing RE, Nair-Gill E, Witte ON, et al. (2010) Visualizing cancer and immune cell function with metabolic positron emission tomography. *Current Opinion in Genetics & Development* 20: 100–105. DOI: [10.1016/j.gde.2009.10.008](https://doi.org/10.1016/j.gde.2009.10.008).
14. Krag D, Weaver D, Ashikaga T, et al. (1998) The sentinel node in breast cancer—a multicenter validation study. *New England Journal of Medicine* 339: 941–946. DOI: [10.1056/NEJM199810013391401](https://doi.org/10.1056/NEJM199810013391401).
15. Gommans GM, Gommans E, van der Zant FM, et al. (2009) ^{99m}Tc Nanocoll: a radiopharmaceutical for sentinel node localisation in breast cancer—in vitro and in vivo results. *Applied Radiation and Isotopes* 67: 1550–1558. DOI: [10.1016/j.apradiso.2009.02.091](https://doi.org/10.1016/j.apradiso.2009.02.091).
16. Taylor ME (2001) Structure and function of the macrophage mannose receptor. *Results and Problems in Cell Differentiation* 33: 105–121.
17. Taylor ME, Conary JT, Lennartz MR, et al. (1990) Primary structure of the mannose receptor contains multiple motifs resembling carbohydrate-recognition domains. *Journal of Biological Chemistry* 265: 12156–12162.
18. Qiao H, Bai J, Chen Y, et al. (2007) Kidney modelling for FDG excretion with PET. *International Journal of Biomedical Imaging* 2007: 1–4. DOI: [10.1155/2007/63234](https://doi.org/10.1155/2007/63234).
19. Vaquero JJ and Kinahan P (2015) Positron emission tomography: current challenges and opportunities for technological advances in clinical and preclinical imaging systems. *Annual Review of Biomedical Engineering* 17: 385–414. DOI: [10.1146/annurev-bioeng-071114-040723](https://doi.org/10.1146/annurev-bioeng-071114-040723).
20. Mariani G, Bruselli L, Kuwert T, et al. (2010) A review on the clinical uses of SPECT/CT. *European Journal of Nuclear Medicine and Molecular Imaging* 37: 1959–1985. DOI: [10.1007/s00259-010-1390-8](https://doi.org/10.1007/s00259-010-1390-8).
21. Garbarino S, Vivaldi V, Delbary F, et al. (2015) A new compartmental method for the analysis of liver FDG kinetics in small animal models. *EJNMMI Research* 5, 107. DOI: [10.1186/s13550-015-0107-1](https://doi.org/10.1186/s13550-015-0107-1).
22. Hays MT and Segall GM (1999) A mathematical model for the distribution of fluorodeoxyglucose in humans. *Journal of Nuclear Medicine* 40: 1358–1366.
23. Delbary F, Garbarino S and Vivaldi V (2016) Compartmental analysis of dynamic nuclear medicine data: models and identifiability. *Inverse Problems* 32, 125010. DOI: [10.1088/0266-5611/32/12/125010](https://doi.org/10.1088/0266-5611/32/12/125010).
24. Moran JK, Lee HB and Blaurock MD (1999) Optimization of urinary FDG excretion during PET imaging. *Journal of Nuclear Medicine* 40: 1352–1357.
25. Bouchet LG, Bolch WE, Blanco HP, et al. (2003) MIRD pamphlet no. 19: absorbed fractions and radionuclide S values for six age-dependent multiregion models of the kidney. *Journal of Nuclear Medicine* 44: 1113–1147.
26. Dorraji SE, Hovd AK, Kanapathippillai P, et al. (2018) Mesenchymal stem cells and T cells in the formation of Tertiary Lymphoid Structures in Lupus Nephritis. *Scientific Reports* 8: 7861. DOI: [10.1038/s41598-018-26265-z](https://doi.org/10.1038/s41598-018-26265-z).
27. Kang S, Fedoriw Y, Brenneman EK, et al. (2017) BAFF induces tertiary lymphoid structures and positions T cells within the glomeruli during lupus nephritis. *The Journal of Immunology* 198: 2602–2611. DOI: [10.4049/jimmunol.1600281](https://doi.org/10.4049/jimmunol.1600281).
28. Dorraji SE, Kanapathippillai P, Karlssen Hovd AM, et al. (2020) Kidney tertiary lymphoid structures in Lupus Nephritis develop into large interconnected networks and resemble lymph nodes in gene signature. *The American Journal of Pathology* 190: 2203–2225. DOI: [10.1016/j.ajpath.2020.07.015](https://doi.org/10.1016/j.ajpath.2020.07.015).
29. Neyt K, Perros F, GeurtsvanKessel CH, et al. (2012) Tertiary lymphoid organs in infection and autoimmunity. *Trends in Immunology* 33: 297–305. DOI: [10.1016/j.it.2012.04.006](https://doi.org/10.1016/j.it.2012.04.006).
30. Corsiero E, Nerviani A, Bombardieri M, et al. (2016) Ectopic lymphoid structures: powerhouse of autoimmunity. *Frontiers in Immunology* 7: 430. DOI: [10.3389/fimmu.2016.00430](https://doi.org/10.3389/fimmu.2016.00430).
31. Blum KS and Pabst R (2006) Keystones in lymph node development. *Journal of Anatomy* 209: 585–595. DOI: [10.1111/j.1469-7580.2006.00650.x](https://doi.org/10.1111/j.1469-7580.2006.00650.x).
32. Rekvig OP, Moens U, Sundsfjord A, et al. (1997) Experimental expression in mice and spontaneous expression in human SLE of polyomavirus T-antigen. A molecular basis for induction of antibodies to DNA and eukaryotic transcription factors. *Journal of Clinical Investigation* 99: 2045–2054.
33. Garbarino S, Caviglia G, Sambuceti G, et al. (2014) A novel description of FDG excretion in the renal system: application to metformin-treated models. *Physics in Medicine and Biology* 59: 2469–2484. DOI: [10.1088/0031-9155/59/10/2469](https://doi.org/10.1088/0031-9155/59/10/2469).

34. Kimura Y, Naganawa M, Shidahara M, et al. (2007) PET kinetic analysis –pitfalls and a solution for the Logan plot. *Annals of Nuclear Medicine* 21: 1–8.
35. Kanapathipillai P, Hedberg A, Fenton CG, et al. (2013) Nucleosomes contribute to increase mesangial cell chemokine expression during the development of lupus nephritis. *Cytokine* 62: 244–252. DOI: [10.1016/j.cyto.2013.03.016](https://doi.org/10.1016/j.cyto.2013.03.016).
36. Davidson A (2016) What is damaging the kidney in lupus nephritis? *Nature Reviews Rheumatology* 12: 143–153. DOI: [10.1038/nrrheum.2015.159](https://doi.org/10.1038/nrrheum.2015.159).
37. Lech M and Anders HJ (2013) The pathogenesis of lupus nephritis. *Journal of the American Society of Nephrology* 24: 1357–1366. DOI: [10.1681/ASN.2013010026](https://doi.org/10.1681/ASN.2013010026).
38. Kurts C, Panzer U, Anders HJ, et al. (2013) The immune system and kidney disease: basic concepts and clinical implications. *Nature Reviews Immunology* 13: 738–753. DOI: [10.1038/nri3523](https://doi.org/10.1038/nri3523).
39. Chang A, Henderson SG, Brandt D, et al. (2011) In situ B cell-mediated immune responses and tubulointerstitial inflammation in human lupus nephritis. *The Journal of Immunology* 186: 1849–1860.
40. Shen Y, Sun CY, Wu FX, et al. (2012) Association of intrarenal B-cell infiltrates with clinical outcome in lupus nephritis: a study of 192 cases. *Clinical and Developmental Immunology* 2012: 1–7. DOI: [10.1155/2012/967584](https://doi.org/10.1155/2012/967584).
41. Russell PS, Hong J, Windsor JA, et al. (2019) Renal lymphatics: anatomy, physiology, and clinical implications. *Frontiers in Physiology* 10: 251. DOI: [10.3389/fphys.2019.00251](https://doi.org/10.3389/fphys.2019.00251).
42. Ruddle NH (2014) Lymphatic vessels and tertiary lymphoid organs. *Journal of Clinical Investigation* 124: 953–959. DOI: [10.1172/JCI71611](https://doi.org/10.1172/JCI71611).
43. Moghimi SM and Bonnemain B (1999) Subcutaneous and intravenous delivery of diagnostic agents to the lymphatic system: applications in lymphoscintigraphy and indirect lymphography. *Advanced Drug Delivery Reviews* 37: 295–312.
44. Nunez EG, Faintuch BL, Teodoro R, et al. (2009) Influence of colloid particle profile on sentinel lymph node uptake. *Nuclear Medicine and Biology* 36: 741–747. DOI: [10.1016/j.nucmedbio.2009.04.009](https://doi.org/10.1016/j.nucmedbio.2009.04.009).
45. Wilhelm AJ, Mijnhout GS and Franssen EJ (1999) Radiopharmaceuticals in sentinel lymph-node detection - an overview. *European Journal of Nuclear Medicine* 26: S36–S42.
46. Chen SC, Vassileva G, Kinsley D, et al. (2002) Ectopic expression of the murine chemokines CCL21a and CCL21b induces the formation of lymph node-like structures in pancreas, but not skin, of transgenic mice. *The Journal of Immunology* 168: 1001–1008. DOI: [10.4049/jimmunol.168.3.1001](https://doi.org/10.4049/jimmunol.168.3.1001).
47. Luther SA, Lopez T, Bai W, et al. (2000) BLC expression in pancreatic islets causes B cell recruitment and lymphotoxin-independent lymphoid neogenesis. *Immunity* 12: 471–481. DOI: [10.1016/S1074-7613\(00\)80199-5](https://doi.org/10.1016/S1074-7613(00)80199-5).
48. Fan L, Reilly CR, Luo Y, et al. (2000) Cutting edge: ectopic expression of the chemokine TCA4/SLC is sufficient to trigger lymphoid neogenesis. *The Journal of Immunology* 164: 3955–3959. DOI: [10.4049/jimmunol.164.8.3955](https://doi.org/10.4049/jimmunol.164.8.3955).
49. Kratz A, CamposNeto A, Hanson MS, et al. (1996) Chronic inflammation caused by lymphotoxin is lymphoid neogenesis. *Journal of Experimental Medicine* 183: 1461–1472. DOI: [10.1084/jem.183.4.1461](https://doi.org/10.1084/jem.183.4.1461).
50. Kolb H, Freytag G, Kiesel U, et al. (1980) Spontaneous autoimmune reactions against pancreatic islets in mouse strains with generalized autoimmune disease. *Diabetologia* 19: 216–221.
51. Limwattana S, Dissaneewate P, Kritsaneepaiboon S, et al. (2013) Systemic lupus erythematosus-related pancreatitis in children. *Clinical Rheumatology* 32: 913–918. DOI: [10.1007/s10067-013-2242-2](https://doi.org/10.1007/s10067-013-2242-2).
52. Saito T, Nishimori I, Miyaji E, et al. (2004) Autoimmune pancreatitis as an initial manifestation of systemic lupus erythematosus. *Modern Rheumatology* 14: 309–313. DOI: [10.3109/s10165-004-0315-4](https://doi.org/10.3109/s10165-004-0315-4).
53. Dhir V, Misra R, Agarwal V, et al. (2011) Lupus pancreatitis - early manifestation of active disease. *Lupus* 20: 547–548. DOI: [10.1177/0961203310385165](https://doi.org/10.1177/0961203310385165).
54. Parungo CP, Soybel DI, Colson YL, et al. (2007) Lymphatic drainage of the peritoneal space: a pattern dependent on bowel lymphatics. *Annals of Surgical Oncology* 14: 286–298. DOI: [10.1245/s10434-006-9044-6](https://doi.org/10.1245/s10434-006-9044-6).